



Cite this: *Nanoscale Adv.*, 2020, **2**, 4106

## Barrier-assisted vapor phase CVD of large-area MoS<sub>2</sub> monolayers with high spatial homogeneity†

Santhosh Durairaj,<sup>a</sup> P. Krishnamoorthy,<sup>a</sup> Navanya Raveendran,<sup>a</sup> Beo Deul Ryu,<sup>b</sup> Chang-Hee Hong,<sup>b</sup> Tae Hoon Seo<sup>c</sup> and S. Chandramohan   <sup>\*</sup>a

Atomically thin molybdenum disulphide (MoS<sub>2</sub>) is a direct band gap semiconductor with negatively charged trions and stable excitons in striking contrast to the wonder material graphene. While large-area growth of MoS<sub>2</sub> can be readily achieved by gas-phase chemical vapor deposition (CVD), growth of continuous MoS<sub>2</sub> atomic layers with good homogeneity is indeed one of the major challenges in vapor-phase CVD involving all-solid precursors. In this study, we demonstrate the growth of large-area continuous single crystal MoS<sub>2</sub> monolayers on *c*-plane sapphire by carefully positioning the substrate using a facile staircase-like barrier. The barrier offered great control in mitigating the secondary and intermediate phases as well as second layer nucleation, and eventually a continuous monolayer with high surface homogeneity is realized. Both micro-Raman and high-resolution transmission electron microscopy (HRTEM) results confirmed the high structural quality of the grown MoS<sub>2</sub> layers. Using low temperature photoluminescence spectroscopy, additional pieces of information are provided for the strong band-edge emission in the light of vacancy compensation and formation of Mo–O bonding. The monolayer MoS<sub>2</sub> transferred to SiO<sub>2</sub>/Si exhibited a room temperature field-effect mobility of  $\sim 1.2 \text{ cm}^2 \text{ V}^{-1} \text{ s}^{-1}$  in a back-gated two-terminal configuration.

Received 21st March 2020  
Accepted 9th July 2020

DOI: 10.1039/d0na00524j  
[rsc.li/nanoscale-advances](http://rsc.li/nanoscale-advances)

## Introduction

Two-dimensional (2D) layered materials are currently at the forefront of various research areas due to their unprecedented properties. Graphene, the first 2D material experimentally realized, has already undergone manifold theoretical and experimental investigations during the last one decade for application in various fields.<sup>1–3</sup> Meanwhile, several other 2D layered materials have been predicted and some are realized experimentally, paving the way for advanced devices with greater functionalities.<sup>2,3</sup> Unlike graphene, monolayer transition metal dichalcogenides (TMDCs) such as MoS<sub>2</sub>, WS<sub>2</sub>, and WSe<sub>2</sub> offer a finite direct band gap, thus showing great potential for application in nano-electronic and optoelectronic devices.<sup>4,5</sup> Molybdenum disulphide (MoS<sub>2</sub>) is one of the TMDCs of current research focus. In MoS<sub>2</sub>, Mo atoms are sandwiched between two sulfur atoms (S–Mo–S) by a strong covalent bond in one of the three structural polytypes, subject to the coordination models between the metal and the chalcogen atoms and stacking orders

between the layers. One of the intriguing characteristics of MoS<sub>2</sub> is the transformation of the optical band gap from indirect (1.2 eV) to direct (1.85 eV) nature with decreasing layer numbers from bulk to the monolayer.<sup>6</sup> In addition, monolayer MoS<sub>2</sub> differs from graphene in two aspects; the first is lack of inversion symmetry which leads to high inter-band transition at the *K*-point due to the valley dependent optical selection rule and the second is the strong spin–orbital coupling in the d-orbital system.<sup>7</sup> Hence, monolayer MoS<sub>2</sub> is considered a potential candidate material for various opto-electronic device applications.<sup>8</sup>

Continuous MoS<sub>2</sub> films with high spatial homogeneity over large areas are the ideal materials for realizing practical devices. Both mechanical<sup>9</sup> and liquid phase exfoliation<sup>10,11</sup> methods are not suitable for electronic device applications because these methods only offer flakes of nano- to micro-meter sizes with poor layer controllability. Alternatively, chemical vapor deposition (CVD) is proven to be a suitable method to grow single crystal MoS<sub>2</sub> with layer controllability and homogeneity over large area.<sup>12–14</sup> Based on the type of precursor used, CVD reactions can be classified as gas phase and vapor phase, and most of the current CVD based MoS<sub>2</sub> production uses either of these two methods. In the gas phase CVD approach, pyrolysis of Mo based hexacarbonyl or organometallic compounds and hydrogen sulphide (H<sub>2</sub>S) occurs on the substrate in a reaction chamber, resulting in continuous MoS<sub>2</sub> on a wafer scale with atomically smooth surfaces.<sup>14–17</sup> Though this method is considered promising for the growth of wafer-scale MoS<sub>2</sub>, the

<sup>a</sup>2D Materials and Devices Laboratory, Department of Physics and Nanotechnology, SRM Institute of Science and Technology, Kattankulathur, 603 203, Tamil Nadu, India. E-mail: chandras3@srmist.edu.in; scmphysics@gmail.com

<sup>b</sup>Department of Semiconductor Science and Technology, Semiconductor Physics Research Center, Chonbuk National University, Jeonju 54896, South Korea

<sup>c</sup>Smart Energy & Nanophotonics R&D Group, Korea Institute of Industrial Technology, Gwangju 61012, South Korea

† Electronic supplementary information (ESI) available. See DOI: [10.1039/d0na00524j](https://doi.org/10.1039/d0na00524j)



high price of the Mo precursors and the need for safety systems to handle certain toxic precursors make this method costly and environmentally not benign. Alternatively, the use of solid phase precursors such as molybdenum trioxide ( $\text{MoO}_3$ ) and sulfur to grow  $\text{MoS}_2$  films has attracted significant attention as these precursors are environmentally friendly and the growth setup is simple and relatively low cost.<sup>12,18,19</sup> Yet another promising feature of this method compared to gas-phase CVD is the ability to achieve larger size grains (up to a few hundreds of micrometers).<sup>20</sup> In fact, this method has been found to be highly effective in achieving rapid growth of other TMDCs such as  $\text{WS}_2$  and  $\text{WSe}_2$  on Au foils.<sup>21,22</sup> Recently, growth of 6 inch uniform  $\text{MoS}_2$  on a glass substrate has been demonstrated *via* a Mo foil-assisted face-to-face metal precursor supply strategy in a vapor-phase CVD process, exploiting the homogeneously distributed Na catalysts in the glass.<sup>23</sup> However, as far as the growth on other substrates is concerned using all-solid precursors, difficulty in controlling the vapor flux (associated with the large difference in the evaporation temperatures of Mo and S source materials) poses challenges in achieving a continuous monolayer  $\text{MoS}_2$  film without secondary or intermediate phases *viz.* molybdenum dioxide ( $\text{MoO}_2$ ) and molybdenum oxsulphide ( $\text{MoOS}_2$ ). These secondary phases have been observed to be present on the surface of  $\text{MoS}_2$  films grown by vapor phase CVD.<sup>24</sup> Several approaches have been used to obtain continuous, large area  $\text{MoS}_2$ , but no control over the formation of secondary phases is realized. Pondick *et al.*<sup>24</sup> reported that both  $\text{MoO}_2$  and  $\text{MoOS}_2$  are intermediate products in a reaction resulting due to variations in the local Mo : S vapor ratio on the substrate. Though this study has shown a way to convert  $\text{MoOS}_2$  into  $\text{MoS}_2$  *via* extended sulfurization by keeping the S : Mo molar ratio well in excess than the stoichiometric requirement, the formation of continuous monolayer  $\text{MoS}_2$  was not demonstrated. To effectively control the precursor reaction rate, Lim *et al.*<sup>25</sup> used nickel oxide (NiO) foam as a reactive-barrier between the  $\text{MoO}_3$  source and the substrate. In this case, the NiO reacts with the  $\text{MoO}_3$  and forms nickel(II) molybdate ( $\text{NiMoO}_4$ ) all along the vapor trajectory in the NiO foam, which eventually controls the Mo concentration gradient. The use of the NiO reactive barrier facilitated the growth of larger grains of  $\sim 170\text{ }\mu\text{m}$  in size on a *c*-plane sapphire substrate, but yet the sample contained a significant amount of secondary phases such as  $\text{MoO}_{3-x}$ . Recently, the use of independent carrier gas pathways and addition of oxygen led to successful wafer-scale epitaxial growth of continuous  $\text{MoS}_2$  on sapphire.<sup>26</sup> Besides the growth of wafer-scale  $\text{MoS}_2$  films, a facile method for growing TMDC monolayers with high spatial homogeneity across a large area is highly desired for further scale-up synthesis.

The present study is therefore focused on understanding the position dependence of the  $\text{MoS}_2$  growth *via* process optimization in realizing continuous monolayer  $\text{MoS}_2$  with high spatial homogeneity and electronic quality without any secondary or intermediate phases. The novelty of our study lies in the use of  $\text{SiO}_2$  as a mechanical barrier to moderate the Mo flux so as to allow better controllability and high position selectivity for the growth of homogeneous  $\text{MoS}_2$  monolayers. The study also

uncovers the potential of the oxide barrier substrate as a possible source of oxygen, which plays an important role in enhancing the photoluminescence of  $\text{MoS}_2$ . A high-resolution transmission electron microscopy (HRTEM) study provided direct evidence for the formation of single crystal  $\text{MoS}_2$  with hexagonal symmetry (2H). For a fixed Mo : S precursor ratio, the density of secondary phases in the sample showed high position dependence. Raman, photoluminescence, and X-ray photo-electron spectroscopic techniques were used to verify the number of layers, crystal and optical quality, and chemical environment of the grown  $\text{MoS}_2$  layers. Electrical measurements using two terminal circular transfer length method (CTLM) test structures showed space charge limited current (SPLC) transport at high applied voltages. The method demonstrated in this study can be extended to grow other TMDCs by vapor-phase CVD using all-solid precursors.

## Experimental section

### Growth of $\text{MoS}_2$

The growth of  $\text{MoS}_2$  was performed in a three-zone CVD system using solid precursors under a continuous flow of argon gas. In a typical experiment, 200 mg of sulfur powder (99.9%, Alfa Aesar) and 10 mg of  $\text{MoO}_3$  powder (99.999%, Alfa Aesar) were taken in two separate ceramic boats and placed inside a quartz tube with a distance of separation of 45 cm. The substrate for the growth, *c*-plane (0001) sapphire, was placed above the  $\text{MoO}_3$  powder on  $\text{SiO}_2$ /Si barriers, as illustrated in Fig. 1. Prior to the growth, the tube was evacuated and purged with argon gas three times. The flow rate of argon gas in all our experiments was set at 200 sccm. The temperature of the sulfur and  $\text{MoO}_3$  precursor zones was set at 180 °C and 700–800 °C, respectively. The temperature of the zone where  $\text{MoO}_3$  was placed was gradually increased at a rate of 7 °C per minute. The other zone where the sulfur was placed was set to a temperature of 180 °C. The heating rate of this zone was calculated based on the temperature ramp time of the high temperature zone. After a dwell time of 10 minutes, the reactor was allowed to cool down to room temperature.

### Characterization and device fabrication

An Olympus optical microscope was used to obtain the microscopic picture of the  $\text{MoS}_2$  surface. The images were captured using a 100× objective (numerical aperture of 0.90). Room temperature micro-Raman spectra were acquired using a HORIBA LabRAM HR evolution spectrometer. All the spectra reported were recorded in backscattering geometry using a solid-state laser with a 532 nm excitation wavelength. The laser power and the spot size used were 5 mW and 1  $\mu\text{m}$ , respectively. PL measurements were carried out on a micro-Raman spectrometer using a He–Cd laser (325 nm) as the excitation source. The surface topography of the  $\text{MoS}_2$  film was studied using an atomic force microscope (Park Systems, Korea) in tapping mode. The optical absorbance of the films (on the two-side polished sapphire substrate) was studied using a UV-Vis-NIR spectrometer (Agilent, Cary 5000). HRTEM analysis of



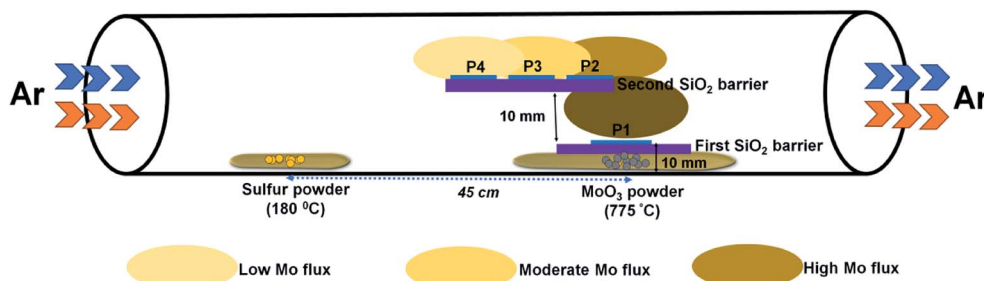


Fig. 1 Schematic of the experimental setup showing the side-view geometry of the stair-case-like barrier and different substrate positions discussed in this work.

the grown  $\text{MoS}_2$  layer was performed using an aberration-corrected electron microscope (JEOL-3010, JEOL, Japan) with a 0.14 nm lattice resolution and 0.12 nm point to point resolution. X-ray photoelectron spectroscopic analyses were performed using a K-Alpha ESCA System (Thermo Scientific) with an  $\text{Al K}\alpha$  (1486.6 eV) X-ray source. Circular TLM and FET devices were fabricated by photolithography followed by metal deposition in a clean room. In a typical CTLM fabrication process, the  $\text{MoS}_2$  sample coated with a negative photoresist was exposed to the i-line (365 nm) through a Cr mask for pattern transfer. The CTLM pattern consisted of ring patterns of varying widths from 5  $\mu\text{m}$  to 45  $\mu\text{m}$ . This was followed by the development step and Ti/Au deposition. For the FET fabrication, the  $\text{MoS}_2$  film was transferred from sapphire to  $\text{p}^{++}$  silicon with a resistivity of 0.01 ohm cm capped with 295 nm thermally grown  $\text{SiO}_2$ . In a typical transfer process, polymethylmethacrylate (PMMA, MW  $\sim$  350k) dissolved in anisole was spin coated at 2000 rpm for 30 s. The  $\text{MoS}_2$  film was then detached in 2 wt% KOH solution at 70 °C for 2 hours and then transferred to successive DI water baths to ensure complete removal of any chemical residues. The floating  $\text{MoS}_2$  film was transferred to the desired substrate and baked for 2 hours at 70 °C. PMMA was removed by immersing the sample in an acetone bath for 2 hours. Back-gated FET devices were defined by photolithography with Ti/Au (30/100 nm) metal as source and drain contact electrodes.  $I$ - $V$  measurements were performed using a LakeShore (Model: PS100) Probe Station and a semiconductor parameter analyzer (Keithley 5200A) at room temperature after evacuating the chamber to a pressure of 5  $\times$  10<sup>-2</sup> mbar.

## Results and discussion

The experimental setup used for the growth of  $\text{MoS}_2$  is schematically illustrated in Fig. 1. Unlike previously reported approaches, where the substrate is placed upside-down directly on the Mo precursor,<sup>27</sup> we used a  $\text{SiO}_2$ /Si substrate as a barrier between the sapphire (growth substrate) and the Mo precursor, and the substrate was placed facing upward. The purpose of this  $\text{SiO}_2$  substrate is to limit the Mo vapor concentration at the substrate position so as to avoid the formation of secondary or intermediate phases. It also helps to understand the position dependence of the growth with respect to the substrate position, as the concentration gradient arises around the Mo source

due to the temperature gradient. From the Mo source position towards the upstream direction, there are three different zones with decreasing Mo flux, as emphasized in Fig. 1. Fig. 2a-c show the optical microscopy images of  $\text{MoS}_2$  grown at 775 °C on sapphire by placing the substrate at position P<sub>1</sub> on the first  $\text{SiO}_2$  barrier (refer to Fig. 1 to visualize the position and see the ESI Fig. S1–S4† for the effect of different growth temperatures). The optical images acquired from different regions of the sample show the presence of grey rod-like structures and white and black particles on the surface. The observed rod-like structures in Fig. 2a are identified as intermediate species of  $\text{MoOS}_2$  by micro-Raman spectroscopy (discussed later), similar to the results reported in ref. 28. It is also observed from the optical images that the local variations in the density of such intermediate species are dependent on the lateral position of the substrate from the Mo precursor. The edge of the substrate which receives the Mo vapor flux first is always found to have higher density of intermediate species. In our experiment, Mo vapors diffuse out from both ends of the substrate, leading to the formation of more intermediate phases on either edge of the substrate along the tube direction, which can be inferred from the colour contrast of the sample shown in Fig. 2d. Raman spectroscopy is a useful tool for qualitative determination of various phases present in the material at the micrometer scale. Fig. 2e shows the Raman spectra obtained for different positions where each spectrum corresponds to the circled position in Fig. 2c with the same colour. The results show the presence of secondary phases such as  $\text{MoO}_2$  and  $\text{MoOS}_2$  on the surface of  $\text{MoS}_2$  with  $\text{MoOS}_2$  being the predominant intermediate phase. The spectrum corresponding to cubic particles shows several peaks; the peaks observed at frequencies below 500  $\text{cm}^{-1}$  match with the stretching modes of oxygen atoms doubly coordinated with Mo atoms (Mo–O–Mo) and the peaks at 574, 594, and 748  $\text{cm}^{-1}$  match with the stretching modes of oxygen terminated Mo, indicating the presence of  $\text{MoO}_2$  crystals in the grown sample.<sup>29</sup> The spectrum corresponding to rod-like structures reveals additional peaks in the frequency range from 384–405  $\text{cm}^{-1}$ , characteristic of Mo=S and S–S vibrations in  $\text{MoOS}_2$ .<sup>24</sup> On the other hand, the spectrum obtained from the smooth region shows the characteristic Raman modes of 2H- $\text{MoS}_2$ , the in-plane-vibration longitudinal optical (LO) phonon mode  $E_{2g}^1$  at 384.2  $\text{cm}^{-1}$  and the out-of-plane-vibration transverse optical (TO) phonon mode  $A_{1g}$  at 404.1  $\text{cm}^{-1}$ . The



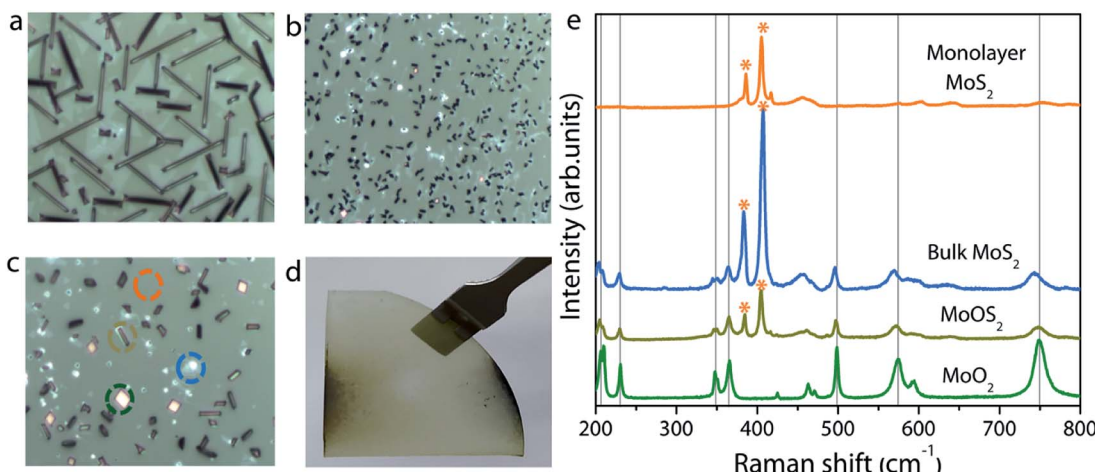


Fig. 2 (a–c) Optical microscopy images of the sample in three different regions from left to right in (d). (d) Photograph of a typical sample grown at position P<sub>1</sub>. (e) Raman spectra of the grown sample at different positions circled in (c) indicating the presence of MoO<sub>2</sub>, MoOS<sub>2</sub>, bulk, and monolayer MoS<sub>2</sub>.

frequency difference ( $\Delta\omega$ ) of  $19.9\text{ cm}^{-1}$  between the two modes confirms the formation of monolayer MoS<sub>2</sub>.<sup>30</sup>

In addition to continuous monolayer formation, the sample showed the formation of bulk MoS<sub>2</sub> at random sites, which is also evident from the Raman spectrum. In the case of bulk MoS<sub>2</sub>, the E<sub>2g</sub><sup>1</sup> mode is shifted towards lower frequency because of long range coulombic interaction force causing the bond length of Mo=S atoms to increase while the A<sub>1g</sub> mode is shifted towards higher frequency due to enhanced restoring force between interlayer S–S bonds.<sup>30</sup> The value of  $\Delta\omega$  in this case is estimated to be  $24.5\text{ cm}^{-1}$ , thus confirming the bulk nature of the MoS<sub>2</sub> in accordance with previous findings.<sup>31</sup> The observed secondary or intermediate phases on the MoS<sub>2</sub> monolayer are

detrimental to the device fabrication. A second barrier is therefore introduced above the first barrier in the form of a staircase to eliminate the secondary phase formation *via* controlling the Mo flux at the substrate position. Fig. 3a–i show the optical images of MoS<sub>2</sub> grown by placing the substrate on the second barrier at three different positions (positions P<sub>2</sub>, P<sub>3</sub>, and P<sub>4</sub> shown in Fig. 1). It is observed that the sample grown by placing the substrate at position P<sub>2</sub> still contains traces of secondary phases, but their density is relatively lower compared to that of the sample grown at P<sub>1</sub>. This result can be understood by considering the high amount of MoO<sub>3</sub> vapors expected at the edge of the barrier. So, the substrate was moved towards the upstream direction in the reactor to position P<sub>3</sub> and P<sub>4</sub> to

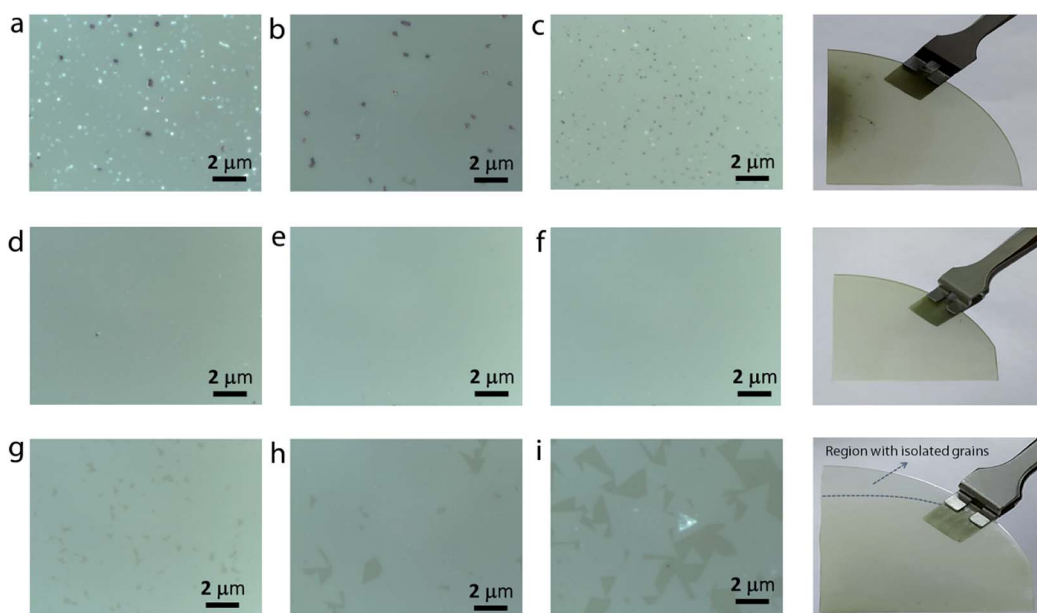


Fig. 3 Optical microscopy images of the MoS<sub>2</sub> sample grown at substrate positions P<sub>2</sub> (a–c), P<sub>3</sub> (d–f) and P<sub>4</sub> (g–i). The three images for each sample are acquired from left, middle, and right portions of the sample. The photographs of the corresponding samples are given on the right.

understand the growth behaviour. At first sight, the sample grown at position  $P_3$  seems to be homogeneous and no obvious colour contrast is seen within the entire grown area (refer to the photograph of the corresponding sample shown on the right). The optical images (Fig. 3d-f) of the sample taken at different points give further indication that the  $\text{MoS}_2$  film is homogeneous on the entire substrate without any secondary or intermediate phases. A further change in the substrate position more towards the upstream direction (at position  $P_4$ ) also provided similar results, except that there was some discontinuity in the film at random sites. In particular, the upstream edge of the substrate had isolated and merged triangular grains (Fig. 3i). Thus, it is presumable that the staircase barrier helped to prevent the direct deposition of secondary phases on the substrate at elevated growth temperature. Also, an increase in the lateral distance between the precursor and the substrate limits the amount of Mo vapors available at the substrate position for the reaction to occur. In all the cases, the Mo : S ratio is fixed to a value of 1 : 20 and the high sulfur content facilitates complete conversion of intermediate phases to  $\text{MoS}_2$ , leading to a homogeneous film formation. The Raman spectrum of the corresponding sample in Fig. 4a shows peaks corresponding to  $E_{2g}^1$  and  $A_{1g}$  at 386.2 and 404.1  $\text{cm}^{-1}$ , respectively. Once again, the  $\Delta\omega$  of 18.9  $\text{cm}^{-1}$  between the two modes suggests the formation of monolayer  $\text{MoS}_2$ . Furthermore, the full width at half maximum (FWHM) of the Raman peak, a figure-of-merit for the qualitative evaluation of the quality of the crystalline structures, is estimated to be 2.9 and 4.2  $\text{cm}^{-1}$ , respectively, for the  $E_{2g}^1$  and  $A_{1g}$  peaks. These values fall within

the range reported for mechanically exfoliated single crystal  $\text{MoS}_2$ , signifying the respectable quality of the grown  $\text{MoS}_2$  layers.<sup>32</sup> The spatial homogeneity of the grown  $\text{MoS}_2$  films is also studied by mapping the positions of the two Raman modes ( $E_{2g}^1$  and  $A_{1g}$ ) over an area of  $30 \times 30 \mu\text{m}^2$  (see also ESI Fig. S5† for the Raman spectrum at various points over the entire substrate). One can visualize from Fig. 4b and c that the frequencies of the two modes are constant at every point the spectrum is acquired with maximum deviation of 0.263  $\text{cm}^{-1}$  and 0.122  $\text{cm}^{-1}$ , respectively, for the  $E_{2g}^1$  and  $A_{1g}$  modes. This result gives further evidence for the homogeneous and monolayer nature of the grown  $\text{MoS}_2$  layers.

The crystal quality and phase purity of the  $\text{MoS}_2$  film are further evaluated with the help of high-resolution transmission electron microscopy (HR-TEM). Fig. 5a shows the low-magnification TEM image of a portion of the sample on a TEM grid. One can clearly see the continuous film with some layer folding, which is inherent to the transfer process. The selected area electron diffraction (SAED) pattern shown in Fig. 5b confirms the single crystalline quality of the grown  $\text{MoS}_2$  layer (see Fig. S6 in the ESI† for SAED patterns obtained from different regions of the sample). Furthermore, the HRTEM image (Fig. 5c) taken at a random site shows the crystal lattice composed of hexagonal rings. Fig. 5d shows the surface topography of typical monolayer  $\text{MoS}_2$  grown at position  $P_3$ . The surface is found to be smooth and homogeneous with a root mean square surface roughness of 0.443 nm. Furthermore, the thickness of the film is estimated to be  $\sim 0.8$  nm (see ESI

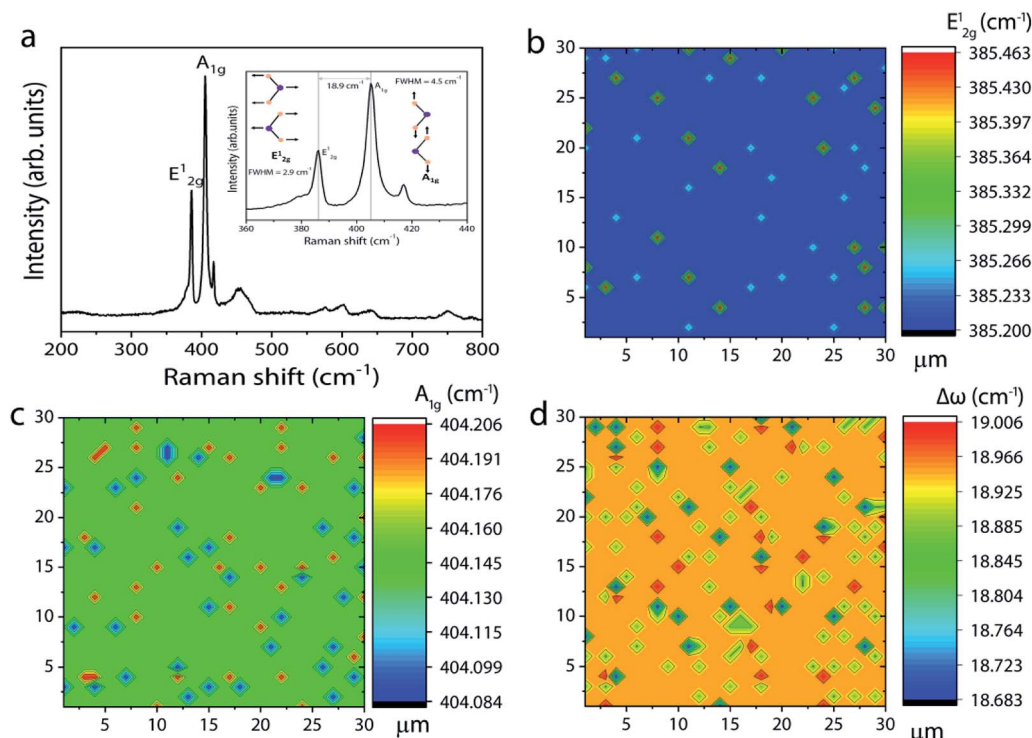


Fig. 4 (a) Raman spectrum of  $\text{MoS}_2$  monolayers grown at position  $P_3$ . The inset shows the same spectrum for  $E_{2g}^1$  and  $A_{1g}$  modes. (b-d) Raman mapping results for  $E_{2g}^1$ ,  $A_{1g}$  and  $\Delta\omega$  frequencies obtained over  $30 \times 30 \mu\text{m}^2$ .

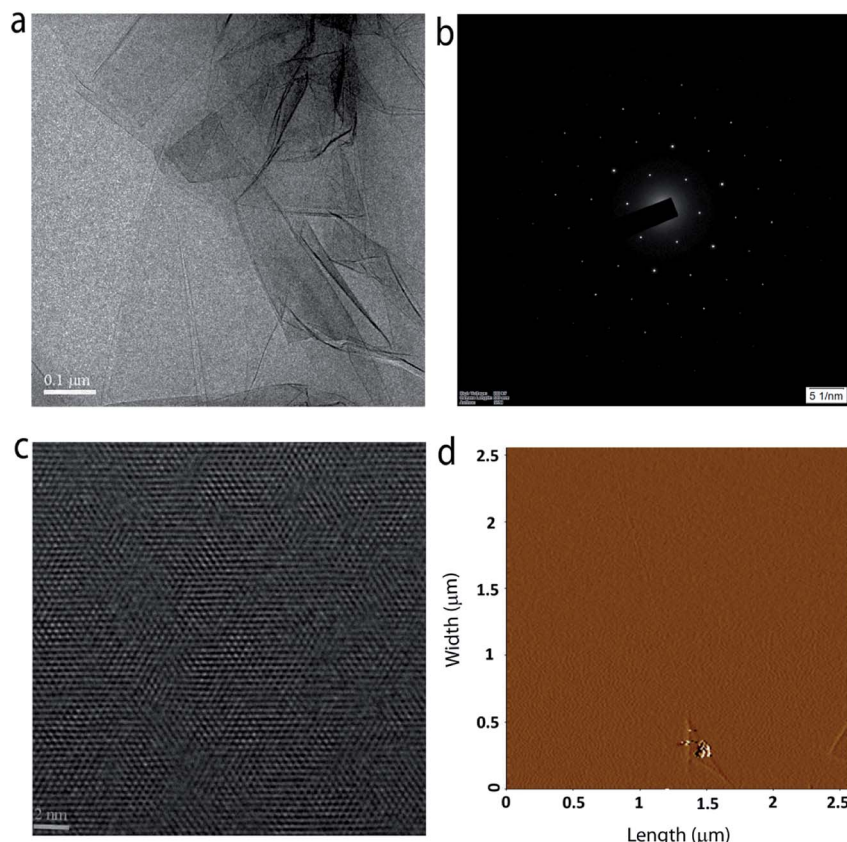


Fig. 5 (a) TEM image of the  $\text{MoS}_2$  film transferred on to a copper grid. (b) SAED pattern indicating the single crystal nature of the grown  $\text{MoS}_2$  film. (c) HRTEM image of the same sample showing the hexagonal structure. (d) AFM surface topography of the grown  $\text{MoS}_2$  film.

Fig. S7†), which is close to the value expected for three atom thick monolayer  $\text{MoS}_2$ .<sup>27</sup>

Photoluminescence measurements were carried out on the  $\text{MoS}_2$  sample grown under optimum conditions. The room-temperature PL spectrum shown in Fig. 6a is characterized by a single strong peak at 1.89 eV, which is attributed to the so-called radiative recombination of neutral A excitons in monolayer  $\text{MoS}_2$ .<sup>6</sup> The low temperature photoluminescence is a unique spectroscopic tool to evaluate the structural defects in semiconducting materials. Fig. 6b shows the PL spectra of a typical monolayer  $\text{MoS}_2$  film recorded at different temperatures from 93 K to 273 K. It is observed that the intensity of the free exciton or band edge ( $X_0$ ) emission increases with decreasing temperature due to better exciton–phonon coupling. Moreover, the exciton peak red shifts as temperature increases due to band gap reduction, a typical trend well described by the Varshni equation for many semiconductors.<sup>33,34</sup> For  $\text{MoS}_2$ , in addition to the free exciton peak, an additional peak at low energy around 1.75 eV arises if bound exciton ( $X_b$ ) states are present.<sup>33–35</sup> If excitons are not tightly bound to defects, they can be easily perturbed by thermal stimulation, and hence a peak evolve at low temperatures. In other words, since the probability for nonradiative recombination increases with temperature, the defect-induced bound exciton peak will quench at room temperature. However, it is interesting to note that the bound exciton peak is not manifest in the spectra even at low

temperatures. According to a study reported by Haiyan Nan *et al.*,<sup>36</sup> oxygen molecules adsorbed on sulfur vacancy sites in the  $\text{MoS}_2$  lattice could enhance the radiative recombination *via* trion-to-exciton conversion and quenching of nonradiative recombination at defect sites (sulfur vacancy sites). As our  $\text{MoS}_2$  samples showed the presence of Mo–O bonding (will be discussed later), the observed strong photoluminescence and the absence of bound exciton peaks both could be taken as a measurement parameter for the high optical quality of the  $\text{MoS}_2$  film. The spatial homogeneity of the sample is further examined by mapping the PL intensities over an area of  $50 \times 50 \mu\text{m}^2$ . Fig. 6c gives a clear picture of the thickness and spatial homogeneity of the grown  $\text{MoS}_2$ . To supplement the PL results, the optical absorption spectrum of the  $\text{MoS}_2$  layer is recorded and the result is shown in Fig. 6d. The spectrum clearly shows three absorption peaks at 1.89, 2.05, and 2.89 eV, corresponding to A, B, and C excitons, respectively. These bands originate from the direct band gap transition in monolayer  $\text{MoS}_2$  at the *K*-point due to spin–orbital coupling induced energy level splitting in the valence band.<sup>6</sup> The energy difference between A and B excitonic peaks is estimated to be 0.16 eV. It is interesting to note that for monolayer  $\text{MoS}_2$  with a high crystal quality and fine electronic structure, this value is reported to be approximately 0.148 eV based on theoretical calculations.<sup>17,37,38</sup> The above result therefore leads us to conclude that the  $\text{MoS}_2$  layers



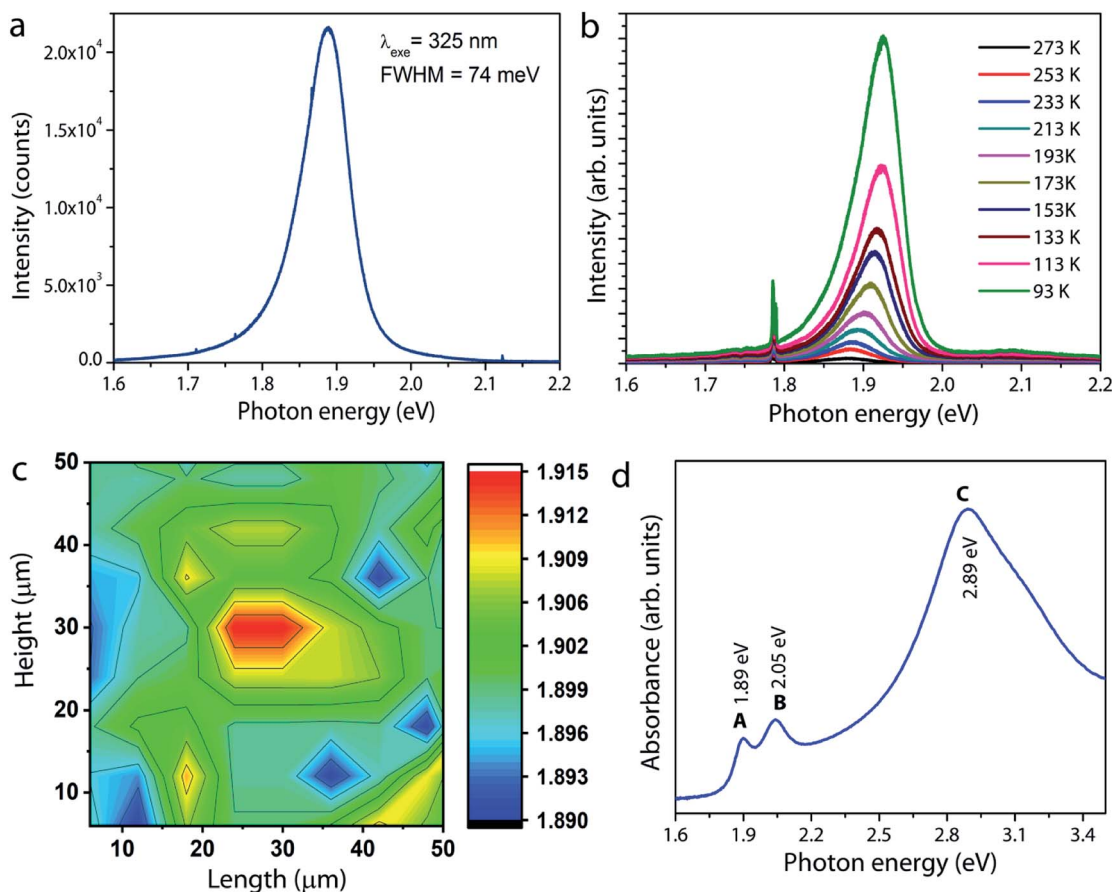


Fig. 6 (a) Room temperature photoluminescence spectrum of  $\text{MoS}_2$  under excitation at 325 nm. (b) Temperature-dependent photoluminescence spectra of the  $\text{MoS}_2$  film. (c) PL mapping for the peak emission wavelength scanned over a  $50 \times 50 \mu\text{m}^2$  area. (d) Absorption spectrum of monolayer  $\text{MoS}_2$ .

grown in this work are of excellent quality, consistent with the HRTEM and PL results.

X-ray photoelectron spectroscopy (XPS) measurements were performed under UHV conditions to examine the atomic composition and nature of the chemical bonding in our  $\text{MoS}_2$  samples. Fig. 7a displays the Mo 3d core level spectrum where the experimental data are fitted with four peaks at a binding energy of 228.8, 231.8, 232.1 and 235.2 eV. The first two peaks,

located at lower binding energies, represent the doublet component  $\text{Mo } 3\text{d}_{5/2}$  and  $\text{Mo } 3\text{d}_{3/2}$  (with a spin-orbit splitting energy of 3 eV) related to  $\text{Mo}^{4+}$  in the sulfur environment. The other two peaks at a higher binding energy of 232.1 and 235.2 eV are attributed to the  $\text{Mo}^{6+} 3\text{d}_{5/2}$  and  $3\text{d}_{3/2}$  doublets of  $\text{MoO}_3$  or substoichiometric  $\text{MoO}_x$  phases.<sup>39–41</sup> This observation indicates the presence of a trace amount of oxygen chemisorbed at sulfur vacancy sites in our  $\text{MoS}_2$  film. Fig. 7b shows the S 2p core-level

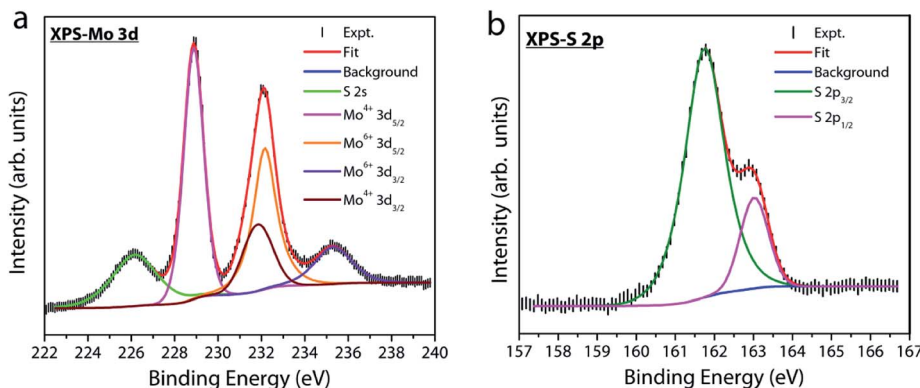


Fig. 7 X-ray photoelectron spectra for (a) Mo 3d and (b) S 2p core-levels. The spectrum was fitted using XPSPEAK4.1 with Shirley background.

spectrum of the  $\text{MoS}_2$  sample. The spectrum is deconvoluted into a single doublet component  $2p_{3/2}$  (161.75 eV) and  $2p_{1/2}$  (163.02 eV). The binding energy position of S 2p confirms that sulfur is in the Mo–S bonding state of  $\text{MoS}_2$ .<sup>39–42</sup> The two different oxidation states for Mo in  $\text{MoS}_2$  grown by solid vapor phase CVD have been previously reported and different reasons have been put forward to explain their origin.<sup>40</sup> Despite the fact that sulfur vacancies when exposed to atmospheric oxygen have a tendency to form  $\text{MoO}_3$  at the surface due to energetic interaction with oxygen,<sup>43</sup> the exact source for the incorporation of oxygen into our sample is unclear. In fact, the  $\text{SiO}_2/\text{Si}$  substrate has been used as a source for supplying continuous oxygen in chemical vapor deposition of graphene.<sup>44</sup> Therefore, release of oxygen from the  $\text{SiO}_2/\text{Si}$  barrier used in our experiments as a source cannot be completely ruled out. This speculation is beyond the scope of this study and requires further experiments and will be reported elsewhere. But, whatever be the source,

sulfur vacancies in  $\text{MoS}_2$  have a tendency to react with oxygen molecules or ions and hence the formation of Mo–O bonds is very probable. The chemisorbed oxygen molecules reoccupying the defect sites in the lattice could increase the quantum yield of free exciton emission,<sup>33,36</sup> which is supported by our PL results discussed earlier.

To understand the carrier transport behaviour in the material without gating effects, a two terminal circular transmission line model (CTLM) device with varying channel length ( $L$ , the gap between the two circular metal contacts) is fabricated by photolithography. Fig. 8a shows the schematic of the device configuration. The current–voltage ( $I$ – $V$ ) curves for different channel lengths measured at lower applied potential are shown in Fig. 8b. It is obvious that the  $I$ – $V$  curves are highly symmetric and linear, except for the deviation observed from linearity above 0.5 volt in the case of  $L = 5 \mu\text{m}$ , which we attribute to the increase in the space charge area in regard to the extent of the

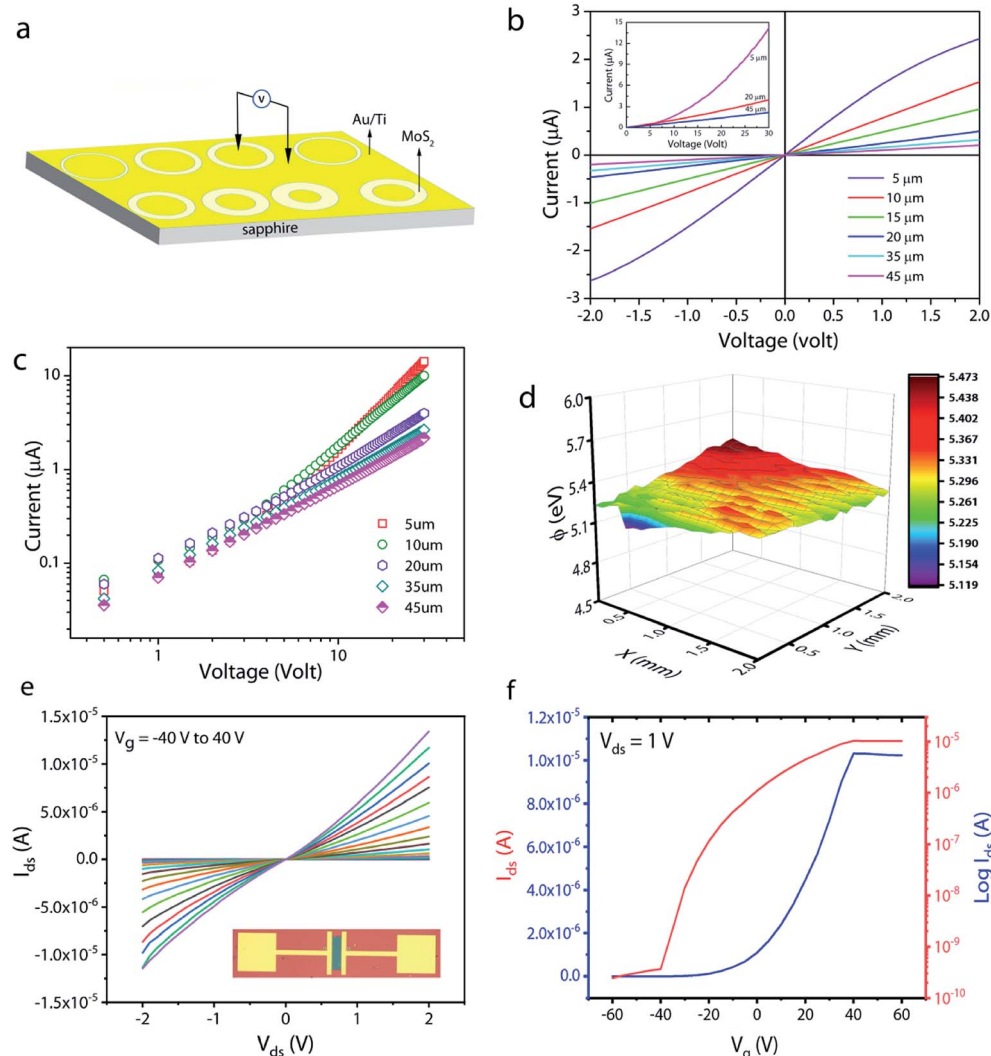


Fig. 8 (a) Schematic of the two-terminal CTLM contact structure used for electrical measurements. (b)  $I$ – $V$  curves obtained for different channel lengths on a linear (b) and (c) log–log scale. (d) Surface work function mapping of  $\text{MoS}_2$  obtained using the scanning Kelvin probe system. (e)  $I_{ds}$ – $V_{ds}$  curves for different gate voltages measured on a back-gated  $\text{MoS}_2$  FET device with a channel width of  $20 \mu\text{m}$ . The inset is the optical image of a typical device. (f) Transfer characteristics of the same device at  $V_{ds} = 1$  volt.



MoS<sub>2</sub> channel, a distinct effect observed particularly at shorter channel lengths. The observed linear *I*-*V* relationship at low applied voltages, on the other hand, reveals the formation of ohmic contact at the Ti/MoS<sub>2</sub> interface due to Fermi level pinning. While the formation of ohmic contact at the Ti/MoS<sub>2</sub> interface is well supported by literature reports,<sup>45–48</sup> the MoS<sub>2</sub> sample appeared to have spatial inhomogeneity in the work function values (which varied from 5.1–5.4 eV), estimated using the scanning Kelvin probe method (Fig. 8d). It has been found that for CVD grown monolayer MoS<sub>2</sub> the high work function appears due to oxygen binding at sulfur vacancies. Such vacancies are shown to favour n-type Ti/MoS<sub>2</sub> contact with a lower Schottky barrier.<sup>47</sup> The scenario of the higher work function due to sulfur vacancies is well corroborated by the existence of a trace amount of the MoO<sub>3</sub> phase in the MoS<sub>2</sub> sample as discussed earlier in the light of the XPS results. The current transport mechanism in MoS<sub>2</sub> is also studied by measuring *I*-*V* characteristics at high applied voltages, as shown in the inset to Fig. 8b. Laskar *et al.*<sup>49</sup> showed that the well-known Mott–Gurney relation for space charge limited current conduction can be applied to thin films with lateral contact geometry, wherein the dependence of current is assumed to take the form  $I \propto \frac{V^2}{L^2}$  instead of  $\propto \frac{V^2}{L^3}$ , where *L* is the channel length. Fig. 8c shows the *I*-*V* curves on a log–log scale where one can clearly see two distinct regions (A and B) for *L* below 10  $\mu\text{m}$ . In region A, the current varies linearly with voltage whereas in region B, it shows quadratic dependence with voltage. This observation indicates the SCLC dominated carrier transport in MoS<sub>2</sub> at high applied voltages. According to previous studies,<sup>43,49</sup> the SCLC region becomes more pronounced at shorter channel lengths and the longitudinal electric field can be realized at relatively low voltages with channel lengths of a few hundred nm. In such devices, the trap states have been identified to have influence on the carrier transport mechanism. In our devices, we found that the SCLC conduction is more pronounced at high applied voltages when the channel length is  $<10 \mu\text{m}$ , consistent with previous findings. For larger channel lengths, the current transport is dominated by ohmic conduction even at high applied voltages, because the overall behaviour of the carrier is still dominated by free charge carrier density. Thus, it is clear that the onset of the SCLC conduction is greatly influenced by the channel length.

In order to further shed light on the electronic quality of the material, back-gated FETs were fabricated by transferring the MoS<sub>2</sub> monolayer to heavily doped p<sup>++</sup> Si capped with thermally grown 295 nm SiO<sub>2</sub>. Fig. 8e and f show the output and transfer curves of a representative device with a channel length and width of 20  $\mu\text{m}$  and 350  $\mu\text{m}$ , respectively. The *I*<sub>ds</sub>-*V*<sub>ds</sub> curves measured for different gate voltages are found to be linear at low ( $<1$  volt) drain voltages, suggesting the ohmic nature of Ti contact, analogous to the CTLM results. Furthermore, the transfer characteristic curve in Fig. 8f shows typical n-type unipolar transport with anticipated transistor behaviour. The field-effect mobility is calculated using the expression  $\mu = \frac{\partial I_{\text{ds}}}{\partial V_g} \left( \frac{L}{WC_{\text{ox}}V_{\text{d}}} \right)$ , where, *I*<sub>ds</sub>, *V*<sub>d</sub>, and *V*<sub>g</sub> denote drain current,

drain voltage, and gate voltage, respectively, and *L* is the channel length, *W* is the channel width, and *C*<sub>ox</sub> is the dielectric capacitance per unit area (defined by  $C_{\text{ox}} = \epsilon_0 \epsilon_r / d$ , where  $\epsilon_0 = 8.854 \times 10^{-12} \text{ F m}^{-1}$ ,  $\epsilon_r$  is dielectric constant of the oxide material (for SiO<sub>2</sub>,  $\epsilon_r = 3.9$ ) and *d* is the thickness of the dielectric film). The average room-temperature mobility is estimated to be about  $1.2 \text{ cm}^2 \text{ V}^{-1} \text{ s}^{-1}$ , which falls within the range of reported mobility values (0.1 to a few tens of  $\text{cm}^2 \text{ V}^{-1} \text{ s}^{-1}$ ) for CVD-grown and exfoliated monolayer MoS<sub>2</sub>.<sup>4,23,25,26,50,51</sup> However, the relatively low mobility observed in our devices compared to recent results reported in ref. 23 and 26 could be due to the wet-transfer process driven poor interface quality at MoS<sub>2</sub>/SiO<sub>2</sub> and metal/MoS<sub>2</sub> interfaces. While the theoretical upper bound of the room temperature mobility for monolayer MoS<sub>2</sub> is predicted to reach a few thousands,<sup>52</sup> the mobility values reported for practical devices are rather low due to intrinsic limitations including the large effective mass of the conduction band and significant phonon scattering, and other factors such as surface impurities, charge traps, intrinsic defects, *etc.* It is proven that sulfur vacancies can limit the carrier mobility by acting as scattering centres for charge carriers and active centres for molecular adsorption or chemical functionalization in the form of impurities.<sup>52,53</sup> However, when oxygen occupies the vacancy sites and forms chemical bonding with Mo (Mo–O), it not only occupies the localized defect states but eventually removes the scattering centres. Based on the low temperature photoluminescence, it has been shown that the carrier mobility has a strong dependence on the  $I_{X_b}/I_{X_0}$  ratio ( $I_{X_0}$  and  $I_{X_b}$  denote the PL intensity of neutral excitons and bound excitons, respectively).<sup>33</sup> It may be recalled once again that since in our samples the X<sub>b</sub> peak was not present, the  $I_{X_b}/I_{X_0}$  value is negligible and hence manifold improvement in charge carrier mobility is possible. We surmise that our MoS<sub>2</sub> films can achieve high field-effect mobility by improving the transfer process and using the high-*k* dielectric environment. The relatively low ( $10^5$  to  $10^6$ ) on/off ratio observed can be attributed to the high off-state current, because Mo–O bonding could likely lead to higher surface carrier concentration.<sup>54</sup>

## Conclusions

In conclusion, large area continuous monolayer MoS<sub>2</sub> films with high homogeneity were achieved by varying the substrate position in vapor phase chemical vapor deposition. The use of a simple mechanical barrier played a key role in controlling the Mo vapor concentration at the substrate position and in yielding homogeneous single crystal MoS<sub>2</sub> with high optical and electronic quality. Optical microscopy and Raman spectroscopy allowed us to precisely determine the different secondary and intermediate phases and their position dependence in the grown MoS<sub>2</sub>. This study provides additional insight into the role of chemisorbed oxygen at sulfur vacancy sites in the photoluminescence characteristics and carrier mobility. The observation of strong photoluminescence suggests that the growth of single crystal continuous MoS<sub>2</sub> using economical and non-toxic precursors demonstrated in this study would lead to the production of high-quality wafer-scale MoS<sub>2</sub> films through



further engineering of the reactor geometry. The method could also be extended to grow other transition metal dichalcogenides on a variety of substrates for the realization of electronic devices.

## Conflicts of interest

There are no conflicts to declare.

## Acknowledgements

SC would like to acknowledge the Science and Engineering Research Board (SERB), Department of Science and Technology, Govt. of India for the Research Grant (YSS/2015/000953). SC sincerely acknowledges SRM Institute of Science and Technology for the seed grant and generous support for the establishment of micro-Raman, UV-Vis-NIR spectrometer, and probe station facilities. Thanks are due to Dr S. Yuvaraj, SRM Institute of Science and Technology, for providing access to SKPM facility (established through research Grant No. ECR/2017/001218).

## Notes and references

- 1 K. S. Novoselov, V. I. Fal, L. Colombo, P. R. Gellert, M. G. Schwab and K. Kim, *Nature*, 2012, **490**, 192.
- 2 F. Withers, O. Del Pozo-Zamudio, A. Mishchenko, A. P. Rooney, A. Gholinia, K. Watanabe, T. Taniguchi, S. J. Haigh, A. K. Geim, A. I. Tartakovskii and K. S. Novoselov, *Nat. Mater.*, 2015, **14**, 301.
- 3 A. C. Ferrari, *et al.*, *Nanoscale*, 2015, **7**, 4598.
- 4 B. Radisavljevic, A. Radenovic, J. Brivio, V. Giacometti and A. Kis, *Nat. Nanotechnol.*, 2011, **6**, 147.
- 5 M. Chhowalla, H. S. Shin, G. Eda, L.-J. Li, K. P. Loh and H. Zhang, *Nat. Chem.*, 2013, **5**, 263.
- 6 K. F. Mak, C. Lee, J. Hone, J. Shan and T. F. Heinz, *Phys. Rev. Lett.*, 2010, **105**, 136805.
- 7 D. Xiao, G.-B. Liu, W. Feng, X. Xu and W. Yao, *Phys. Rev. Lett.*, 2012, **108**, 196802.
- 8 Q. H. Wang, K. Kalantar-Zadeh, A. Kis, J. N. Coleman and M. S. Strano, *Nat. Nanotechnol.*, 2012, **7**, 699.
- 9 A. Splendiani, L. Sun, Y. Zhang, T. Li, J. Kim, C.-Y. Chim, G. Galli and F. Wang, *Nano Lett.*, 2010, **10**, 1271–1275.
- 10 J. N. Coleman, M. Lotya, A. O'Neill, S. D. Bergin, P. J. King, U. Khan, K. Young, A. Gaucher, S. De and R. J. Smith, *Science*, 2011, **331**, 568.
- 11 J. W. Christopher, B. B. Goldberg and A. K. Swan, *Sci. Rep.*, 2017, **7**, 14062.
- 12 D. Li, Z. Xiao, S. Mu, F. Wang, Y. Liu, J. Song, X. Huang, L. Jiang, J. Xiao and L. Liu, *Nano Lett.*, 2018, **18**, 2021–2032.
- 13 K. Kang, S. Xie, L. Huang, Y. Han, P. Y. Huang, K. F. Mak, C.-J. Kim, D. Muller and J. Park, *Nature*, 2015, **520**, 656.
- 14 N. B. Shinde, B. Francis, M. S. Ramachandra Rao, B. D. Ryu, S. Chandramohan and S. K. Eswaran, *APL Mater.*, 2019, **7**, 81113.
- 15 V. K. Kumar, S. Dhar, T. H. Choudhury, S. A. Shivashankar and S. Raghavan, *Nanoscale*, 2015, **7**, 7802–7810.
- 16 A. Gaur, D. Chiappe, D. Lin, D. Cott, I. Asselberghs, M. Heyns and I. Radu, *2D Mater.*, 2019, **6**, 35035.
- 17 C.-C. Huang, F. Al-Saab, Y. Wang, J.-Y. Ou, J. C. Walker, S. Wang, B. Gholipour, R. E. Simpson and D. W. Hewak, *Nanoscale*, 2014, **6**, 12792–12797.
- 18 C. Chen, Z. Feng, Y. Feng, Y. Yue, C. Qin, D. Zhang and W. Feng, *ACS Appl. Mater. Interfaces*, 2016, **8**, 19004–19011.
- 19 B. Chen, Q. Yu, Q. Yang, P. Bao, W. Zhang, L. Lou, W. Zhu and G. Wang, *RSC Adv.*, 2016, **6**, 50306–50314.
- 20 A. Sharma, M. A. Verheijen, L. Wu, S. Karwal, V. Vandalon, H. C. M. Knoops, R. S. Sundaram, J. P. Hofmann, W. M. M. E. Kessels and A. A. Bol, *Nanoscale*, 2018, **10**, 8615–8627.
- 21 Y. Gao, Z. Liu, D.-M. Sun, L. Huang, L.-P. Ma, L.-C. Yin, T. Ma, Z. Zhang, X.-L. Ma and L.-M. Peng, *Nat. Commun.*, 2015, **6**, 8569.
- 22 Y. Gao, Y. Hong, L. Yin, Z. Wu, Z. Yang, M. Chen, Z. Liu, T. Ma, D. Sun and Z. Ni, *Adv. Mater.*, 2017, **29**, 1700990.
- 23 P. Yang, X. Zou, Z. Zhang, *et al.*, *Nat. Commun.*, 2018, **9**, 979.
- 24 J. V. Pondick, J. M. Woods, J. Xing, Y. Zhou and J. J. Cha, *ACS Appl. Nano Mater.*, 2018, **1**, 5655–5661.
- 25 Y.-F. Lim, K. Priyadarshi, F. Bussolotti, P. K. Gogoi, X. Cui, M. Yang, J. Pan, S. W. Tong, S. Wang and S. J. Pennycook, *ACS Nano*, 2018, **12**, 1339–1349.
- 26 H. Yu, M. Liao, W. Zhao, G. Liu, X. J. Zhou, Z. Wei, X. Xu, K. Liu, Z. Hu and K. Deng, *ACS Nano*, 2017, **11**, 12001–12007.
- 27 Z. Lin, Y. Zhao, C. Zhou, R. Zhong, X. Wang, Y. H. Tsang and Y. Chai, *Sci. Rep.*, 2015, **5**, 18596.
- 28 B. Li, S. Yang, N. Huo, Y. Li, J. Yang, R. Li, C. Fan and F. Lu, *RSC Adv.*, 2014, **4**, 26407–26412.
- 29 R. Narro-García, N. Méndez, L. M. Apátiga, J. P. Flores-De los Ríos, C. G. Nava-Dino and R. Quintero-Torres, *Int. J. Electrochem. Sci.*, 2017, **12**, 3907–3915.
- 30 C. Lee, H. Yan, L. E. Brus, T. F. Heinz, J. Hone and S. Ryu, *ACS Nano*, 2010, **4**, 2695–2700.
- 31 H. Li, Q. Zhang, C. C. R. Yap, B. K. Tay, T. H. T. Edwin, A. Olivier and D. Baillargeat, *Adv. Funct. Mater.*, 2012, **22**, 1385–1390.
- 32 B. Chakraborty, H. S. S. R. Matte, A. K. Sood and C. N. R. Rao, *J. Raman Spectrosc.*, 2013, **44**, 92–96.
- 33 H. Nan, Z. Wu, J. Jiang, A. Zafar, Y. You and Z. Ni, *J. Phys. D: Appl. Phys.*, 2017, **50**, 154001.
- 34 T. Korn, S. Heydrich, M. Hirmer, J. Schmutzler and C. Schuller, *Appl. Phys. Lett.*, 2011, **99**, 102109.
- 35 X.-X. Zhang, Y. You, S. Y. F. Zhao and T. F. Heinz, *Phys. Rev. Lett.*, 2015, **115**, 257403.
- 36 H. Nan, Z. Wang, W. Wang, Z. Liang, Y. Lu, Q. Chen, D. He, P. Tan, F. Miao and X. Wang, *ACS Nano*, 2014, **8**, 5738–5745.
- 37 P. J. Ko, A. Abderrahmane, T. V. Thu, D. Ortega, T. Takamura and A. Sandhu, *J. Nanosci. Nanotechnol.*, 2015, **15**, 6843–6846.
- 38 Y. Yu, C. Li, Y. Liu, L. Su, Y. Zhang and L. Cao, *Sci. Rep.*, 2013, **3**, 1866.
- 39 Y. Ho, C. Ma, T. Luong, L. Wei, T. Yen, W. Hsu, W. Chang, Y. Chu, Y. Tu and K. P. Pande, *Phys. Status Solidi RRL*, 2015, **9**, 187–191.



40 G. Deokar, D. Vignaud, R. Arenal, P. Louette and J.-F. Colomer, *Nanotechnol.*, 2016, **27**, 75604.

41 X. Wang, Y. P. Zhang and Z. Q. Chen, *Mater. Res. Express*, 2016, **3**, 65014.

42 C.-R. Wu, X.-R. Chang, C.-H. Wu and S.-Y. Lin, *Sci. Rep.*, 2017, **7**, 42146.

43 S. Ghatak and A. Ghosh, *Appl. Phys. Lett.*, 2013, **103**, 122103.

44 X. Xu, Z. Zhang, L. Qiu, J. Zhuang, L. Zhang, H. Wang, C. Liao, H. Song, R. Qiao and P. Gao, *Nat. Nanotechnol.*, 2016, **11**, 930.

45 I. Popov, G. Seifert and D. Tománek, *Phys. Rev. Lett.*, 2012, **108**, 156802.

46 L. Britnell, R. M. Ribeiro, A. Eckmann, R. Jalil, B. D. Belle, A. Mishchenko, Y.-J. Kim, R. V. Gorbachev, T. Georgiou and S. V. Morozov, *Science*, 2013, **340**, 1311–1314.

47 L. Feng, J. Su, D. Li and Z. Liu, *Phys. Chem. Chem. Phys.*, 2015, **17**, 6700–6704.

48 S. McDonnell, C. Smyth, C. L. Hinkle and R. M. Wallace, *ACS Appl. Mater. Interfaces*, 2016, **8**, 8289–8294.

49 M. R. Laskar, L. Ma, S. Kannappan, P. Sung Park, S. Krishnamoorthy, D. N. Nath, W. Lu, Y. Wu and S. Rajan, *Appl. Phys. Lett.*, 2013, **102**, 252108.

50 M. Amani, M. L. Chin, A. G. Birdwell, T. P. O'Regan, S. Najmaei, Z. Liu, P. M. Ajayan, J. Lou and M. Dubey, *Appl. Phys. Lett.*, 2013, **102**, 193107.

51 N. Huo, Y. Yang, Y.-N. Wu, X.-G. Zhang, S. T. Pantelides and G. Konstantatos, *Nanoscale*, 2018, **10**, 15071–15077.

52 X. Cui, G.-H. Lee, Y. D. Kim, et al., *Nat. Nanotechnol.*, 2015, **10**, 534.

53 A. M. Van Der Zande, P. Y. Huang, D. A. Chenet, T. C. Berkelbach, Y. You, G.-H. Lee, T. F. Heinz, D. R. Reichman, D. A. Muller and J. C. Hone, *Nat. Mater.*, 2013, **12**, 554.

54 T. Zhang, Y. Wang, J. Xu, L. Chen, H. Zhu, Q. Sun, S. Ding and D. W. Zhang, *2D Mater.*, 2017, **5**(1), 015028.

